KSME

Springer

Journal of Mechanical Science and Technology 34 (12) 2020

Original Article
DOI 10.1007/s12206-020-1117-0

Keywords:
· Conjugate curves theory
· Internal gear
· Mathematical principle
· Meshing analysis
· Tooth profiles models

Correspondence to:
Dong Liang
cqjtuliandong_me@163.com

Citation:
Liang, D., Li, D., Chen, B. (2020). Mathematical model and meshing analysis of internal meshing gear transmission with curve element. Journal of Mechanical Science and Technology 34 (12) (2020) 5155~5166.
http://doi.org/10.1007/s12206-020-1117-0

Received December 17th, 2019
Revised August 15th, 2020
Accepted September 9th, 2020

† Recommended by Editor Seungjae Min

Mathematical model and meshing analysis of internal meshing gear transmission with curve element

Dong Liang[1,2], Weibin Li[2] and Bingkui Chen[2]

[1]School of Mechanotronics & Vehicle Engineering, Chongqing Jiaotong University, Chongqing 400074, China, [2]State Key Laboratory of Mechanical Transmission, Chongqing University, Chongqing 400030, China

Abstract A new internal meshing gear transmission with curve element is put forward in this paper. The mathematical principle of tooth profile generation is described based on conjugate curves theory. For a given spatial curve, the meshing equation and its conjugated spatial curve under the motion law were derived. Considering the equidistant kinematic method, general internal tooth profiles models were established by the conjugate-curve pair. Numerical example of the internal gear pair was developed according to gear parameters and gear solid models were established by MATLAB and UG software. Motion simulation result shows that the gear pair satisfies point contact condition and design requirements. Meshing analysis of tooth profiles using FEA method was carried out. Stress analysis results of tooth profiles with single point contact and two points contact were, respectively, obtained. The conclusions lay the foundation for multi-point contact generation and tooth profile design. Also, further studies on transmission characteristics and manufacturing technology of the new gear drive will be carried out.

1. Introduction

Internal meshing gears are widely used in planetary gear transmissions. Compared with external meshing gear transmission, they have the advantages of compact structure, larger transmission ratio, higher load capacity, higher transmission efficiency and better dynamic characteristics [1]. Involute tooth profiles are currently the application object and many studies, such as tooth profile modification, theoretical design, meshing characteristics analysis and manufacturing technology, have been carried out. For example, Litvin [2] described the general principle of the internal involute gears. The problems of undercutting of internal involute gears in the process of generation and interference by their assembly with pinions were analyzed. The kinematics of the process for generation of the gear fillet and investigation of interference by radial assembly of the gear and pinion based on a tooth contact analysis were also introduced. Yang [3] used a double envelope concept to determine the basic profile of an internal gear with asymmetric involute teeth. A mathematical model of the meshing principles of gear pair was presented and gear prototype was manufactured utilizing rapid prototyping and manufacturing technology. Chen [4] developed a novel worm drive consisting of a planar internal gear and a crown worm. Generation process of the internal gear was provided and a new machining method was proposed based on the principle of virtual center distance. Cho [5] introduced a structural analysis method considering the tooth contact of internal gear system for wind turbine gearbox. The actual tooth contact between a pair of gears was modeled with spring elements and the spring constants were determined through the stiffness analysis of gear teeth. Tunalioglu [6] investigated theoretically the wear in internal gears by adapting Archard's wear equation to internal gears and designed and manufactured a fatigue and wear test equipment to investigate wear in internal gears experimentally. Pham [7, 8] studied the start-up (zero load) and the dynamically-loaded behavior of the ring gear in the internal gear

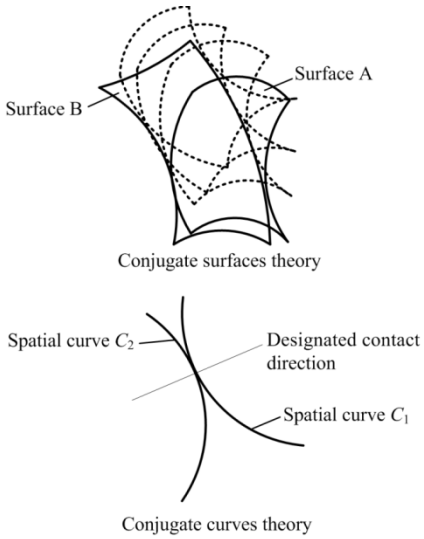

Fig. 1. Comparisons of two theories.

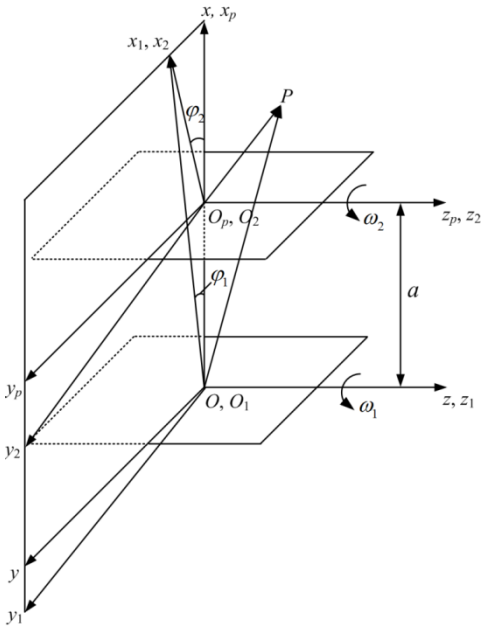

Fig. 2. Coordinate systems of internal meshing gear pair.

motor pump. Moreover, the orbit, the pressure distribution, and thermal behavior of the fluid film were also analyzed. Liu [9] researched gear shaping strategy for internal helical non-circular gears and performance analyses for linkage models. Gui [10] proposed a new internal compound cycloid gear pair with high contact ratio. A mathematical equation of conjugate tooth profile was established and the unification calculation formula of transverse contact ratio suitable for any tooth profile of gear was deduced. Yanase [11] developed a high-precision and high-efficiency method of grinding internal gears, which uses a barrel-shaped threaded grinding wheel to realize a large crossed-axes angle between the internal gear and the grinding wheel. The geometrical and numerical analysis of the grinding method had been also carried out. Uriu [12] analyzed the parameter selection of skiving process for internal gears. The validity of the value of shaft angle was discussed by calculating the cutting tool parameters, such as instantaneous rake angles, clearance angles, cut depths, and cutting speeds at continuously moving cutting points against various shaft angles. Han [13] derived the contact line equation of tooth surface with homogeneous coordinate transformation method. The influence of shaft angle Σ on the formation of surface arc texture of workpiece was analyzed. The three-dimensional profilometer was also utilized to analyze the roughness value with a set of process parameters.

However, two problems for internal involute gears application exist: 1) An internal gear pair is prone to interference effects, such as tooth profile overlap interference, radial interference and transition curve interference. Generally, we use the modification method to overcome the difficult for tooth profile design and calculation. 2) Internal involute gears are usually machined with shaping cutter, and over-cutting and low productivity conditions may happen. Tooth profile hardness and manufacturing accuracy are also limited.

The authors proposed a new design theory for gear transmission based on spatial conjugate curves. General principle, meshing characteristics analysis and manufacturing method of the gears with parallel axes or intersecting axes were studied [14-19]. Whereas, the internal meshing gears are different from general external meshing gears in the aspects of generation principle, design method and manufacturing technology.

In this paper, an internal meshing gear transmission based on curve element is put forward. Generation principle and mathematical model of the gears were developed. Meshing equation of internal conjugate-curve pair in arbitrary contact normal direction was derived and general expressions of tooth profiles were also deduced. Numerical examples of the conjugate-curve pair and tubular tooth surfaces are illustrated according to design parameters. Meshing characteristics analysis of the gear pair is further carried out based on established solid models.

2. Mathematical model of internal gear pair with curve element

2.1 Meshing principle and general equation

Conjugate surface theory at present is the theoretical foundation of gear geometry. Through giving spatial surface A and its motion law, the other spatial surface B, which is conjugated to surface A, can be obtained. Specially, the surface B is unique due to the limitation of spatial position relationship [2]. The proposed conjugate curve theory considering a variety of contact form of the spatial curves shows that the spatial curve C_2 can be got if given a spatial curve C_1 and its designated motion law. It is noteworthy that the spatial curve C_2 is not unique because of the various contact position relationships. The comparisons of two theories are displayed in Fig. 1.

Fig. 2 shows the coordinate systems of internal meshing

gear pair, including the fixed coordinate systems S(O-x, y, z), S_p(O_p-x_p, y_p, z_p), and the movable coordinate systems S_1(O_1-x_1, y_1, z_1), S_2(O_2-x_2, y_2, z_2). ω_1 and ω_2 are rotational angle velocities, which are, respectively, corresponding to gears 1 and 2. φ_1 and φ_2 are the rotational angles of gears 1 and 2 under the given motion. There is a relationship $\varphi_2 = i_{21}\varphi_1$, where i_{21} is transmission ratio. a is central distance and point P is the common contact point of internal gear pair.

We obtained the transformation matrix from coordinate system S_1 to S_2 by using differential geometry [20]. And it has

$$\boldsymbol{M}_{21} = \begin{bmatrix} \cos(\varphi_1-\varphi_2) & -\sin(\varphi_1-\varphi_2) & 0 & -a\cos\varphi_2 \\ \sin(\varphi_1-\varphi_2) & \cos(\varphi_1-\varphi_2) & 0 & a\sin\varphi_2 \\ 0 & 0 & 1 & 0 \\ 0 & 0 & 0 & 1 \end{bmatrix}. \tag{1}$$

Similarly, the transformation matrix from coordinate system S_2 to S_1 can be obtained as follows.

$$\boldsymbol{M}_{12} = \begin{bmatrix} \cos(\varphi_1-\varphi_2) & \sin(\varphi_1-\varphi_2) & 0 & a\cos\varphi_1 \\ -\sin(\varphi_1-\varphi_2) & \cos(\varphi_1-\varphi_2) & 0 & -a\sin\varphi_1 \\ 0 & 0 & 1 & 0 \\ 0 & 0 & 0 & 1 \end{bmatrix}. \tag{2}$$

According to kinematics methods, the relative velocity of the gears at point P is calculated as

$$\boldsymbol{v}_1^{(12)} = \boldsymbol{v}_1^{(1)} - \boldsymbol{v}_1^{(2)} \tag{3}$$

where $\boldsymbol{v}_1^{(1)}$ and $\boldsymbol{v}_1^{(2)}$ are the velocity of gears 1 and 2 at point P under coordinate system S_1.

The velocity $\boldsymbol{v}_1^{(1)}$ can be expressed with

$$\boldsymbol{v}_1^{(1)} = \boldsymbol{\omega}^{(1)} \times \boldsymbol{r}_1 . \tag{4}$$

and the velocity $\boldsymbol{v}_1^{(2)}$ is written as

$$\boldsymbol{v}_1^{(2)} = \boldsymbol{\omega}_1^{(2)} \times \boldsymbol{r}_1 + \boldsymbol{a} \times \boldsymbol{\omega}^{(2)} \tag{5}$$

where

$$\begin{aligned} &\boldsymbol{r}_1 = \overrightarrow{O_1P} = x_1\boldsymbol{i}_1 + y_1\boldsymbol{j}_1 + z_1\boldsymbol{k}_1 \\ &\boldsymbol{a} = \overrightarrow{O_1O_2} = a\cos\varphi_1\boldsymbol{i}_1 - a\sin\varphi_1\boldsymbol{j}_1 \\ &\boldsymbol{\omega}^{(1)} = \omega_1\boldsymbol{k}_1 \\ &\boldsymbol{\omega}_1^{(2)} = \boldsymbol{\omega}^{(2)} = \omega_2\boldsymbol{k}_1 . \end{aligned}$$

$\boldsymbol{r}_1$ is the vector of spatial curve 1. $\boldsymbol{i}_1$, $\boldsymbol{j}_1$ and $\boldsymbol{k}_1$ are the unit vectors corresponding to the coordinate axes x_1, y_1 and z_1, respectively.

Subscribing Eqs. (4) and (5) into Eq. (3), we have

$$\begin{aligned} \boldsymbol{v}_1^{(12)} = &[-(\omega_1-\omega_2)y_1 + \omega_2 a\sin\varphi_1]\boldsymbol{i}_1 \\ &+[(\omega_1-\omega_2)x_1 + \omega_2 a\cos\varphi_1]\boldsymbol{j}_1 . \end{aligned} \tag{6}$$

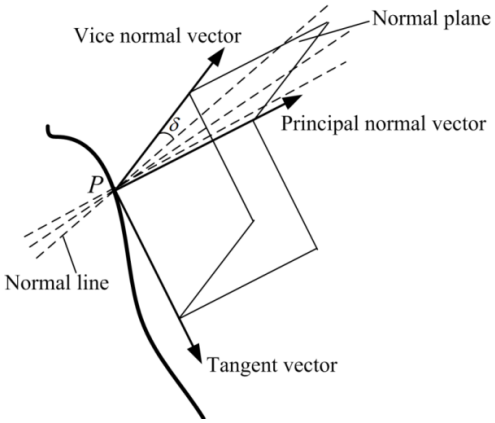

Fig. 3. Space curve trihedron.

Furthermore, normal vector $\boldsymbol{n}$ will be derived based on the space curve trihedron in Fig. 3. Three perpendicular vectors for spatial curves at any contact point are the principal normal vector, vice normal vector and tangent vector. Obviously, a normal plane is formed based on the principal normal vector and vice normal vector. Normal lines located on the normal plane have different directions at point P. Here, we define the parameter δ as the angle between normal line and vice normal vector. So normal vector $\boldsymbol{n}$ in arbitrary contact direction is expressed with the following meaning:

$$\boldsymbol{n} = \lambda_1\boldsymbol{n}_{pn} + \lambda_2\boldsymbol{n}_{vn} \tag{7}$$

where λ_1 and λ_2 are the parameters which determine the direction of designated normal line. There are $\lambda_1 = U\sin\delta$ and $\lambda_2 = U\cos\delta$, U is the unit vector length.

Under coordinate system S_1, it can be written as

$$\begin{aligned} \boldsymbol{n}_1 = &(\lambda_1\boldsymbol{n}_{pn1x} + \lambda_2\boldsymbol{n}_{vn1x})\boldsymbol{i}_1 + (\lambda_1\boldsymbol{n}_{pn1y} + \lambda_2\boldsymbol{n}_{vn1y})\boldsymbol{j}_1 \\ &+ (\lambda_1\boldsymbol{n}_{pn1z} + \lambda_2\boldsymbol{n}_{vn1z})\boldsymbol{k}_1 . \end{aligned} \tag{8}$$

Here,

$$\begin{cases} \boldsymbol{n}_{pn1x} = \dfrac{x''(t)[y'^2(t)+z'^2(t)] - x'(t)[y'(t)y''(t)+z'(t)z''(t)]}{[x'^2(t)+y'^2(t)+z'^2(t)]^2} \\ \boldsymbol{n}_{pn1y} = \dfrac{y''(t)[x'^2(t)+z'^2(t)] - y'(t)[x'(t)x''(t)+z'(t)z''(t)]}{[x'^2(t)+y'^2(t)+z'^2(t)]^2} \\ \boldsymbol{n}_{pn1z} = \dfrac{z''(t)[x'^2(t)+y'^2(t)] - z'(t)[x'(t)x''(t)+y'(t)y''(t)]}{[x'^2(t)+y'^2(t)+z'^2(t)]^2} \end{cases},$$

and

$$\begin{cases} \boldsymbol{n}_{vn1x} = \dfrac{y'(t)z''(t) - z'(t)y''(t)}{[x'^2(t)+y'^2(t)+z'^2(t)]^{3/2}} \\ \boldsymbol{n}_{vn1y} = -\dfrac{x'(t)z''(t) - z'(t)x''(t)}{[x'^2(t)+y'^2(t)+z'^2(t)]^{3/2}} \\ \boldsymbol{n}_{vn1z} = \dfrac{x'(t)y''(t) - y'(t)x''(t)}{[x'^2(t)+y'^2(t)+z'^2(t)]^{3/2}} \end{cases},$$

t is curve parameter.

Usually, the meshing equation is derived using the relationships of the relative velocity ***v*** and normal vector ***n***, and it has

$$\begin{aligned}\Phi = \boldsymbol{n}_1 \cdot \boldsymbol{v}_1^{(12)} &= [-(\omega_1-\omega_2)y_1 + \omega_2 a\sin\varphi_1](\lambda_1\boldsymbol{n}_{pn1x} + \lambda_2\boldsymbol{n}_{vn1x}) \\ &+ [(\omega_1-\omega_2)x_1 + \omega_2 a\cos\varphi_1](\lambda_1\boldsymbol{n}_{pn1y} + \lambda_2\boldsymbol{n}_{vn1y}) \\ &= 0 .\end{aligned} \tag{9}$$

Eq. (9) can be further simplified due to the relationship $i_{21} = \omega_2/\omega_1$. So it is rewritten as

$$\begin{aligned}&i_{21}a(\lambda_1\boldsymbol{n}_{pn1y} + \lambda_2\boldsymbol{n}_{vn1y})\cos\varphi_1 + i_{21}a(\lambda_1\boldsymbol{n}_{pn1x} + \lambda_2\boldsymbol{n}_{vn1x})\sin\varphi_1 \\ &-(1-i_{21})[y_1(\lambda_1\boldsymbol{n}_{pn1x} + \lambda_2\boldsymbol{n}_{vn1x}) - x_1(\lambda_1\boldsymbol{n}_{pn1y} + \lambda_2\boldsymbol{n}_{vn1y})] = 0 .\end{aligned} \tag{10}$$

Assumed that

$$\begin{aligned}A_1 &= i_{21}a(\lambda_1\boldsymbol{n}_{pn1y} + \lambda_2\boldsymbol{n}_{vn1y}) \\ A_2 &= -i_{21}a(\lambda_1\boldsymbol{n}_{pn1x} + \lambda_2\boldsymbol{n}_{vn1x}) \\ A_3 &= (1-i_{21})[y_1(\lambda_1\boldsymbol{n}_{pn1x} + \lambda_2\boldsymbol{n}_{vn1x}) - x_1(\lambda_1\boldsymbol{n}_{pn1y} + \lambda_2\boldsymbol{n}_{vn1y})] ,\end{aligned}$$

then we can express the Eq. (10) into

$$A_1\cos\varphi_1 - A_2\sin\varphi_1 = A_3 . \tag{11}$$

Considering the meshing equation and transformation relationship between coordinate systems S_1 and S_2, we get the conjugated spatial curve 2 in the direction of arbitrary normal vector as follows.

$$\begin{cases}\boldsymbol{r}_2 = \boldsymbol{M}_{21}\boldsymbol{r}_1 \\ A_1\cos\varphi_1 - A_2\sin\varphi_1 = A_3 .\end{cases} \tag{12}$$

To verify above conclusions, numerical examples for internal meshing conjugate-curve pair are provided using plane involute and spatial cylindrical helical curve, respectively.

(1) Plane involute

Suppose that plane involute C_1 is located on gear 1, the equation is written as

$$\begin{cases}x_{i1} = R_b\cos\theta + R_b\theta\sin\theta \\ y_{i1} = R_b\sin\theta - R_b\theta\cos\theta \\ z_{i1} = 0\end{cases} \tag{13}$$

where R_b is basis circle radius and θ is involute parameter angle. According to the aforementioned conclusions, we can derive the meshing equation and its simplified result is

$$\cos(\varphi_1+\theta) - \frac{(i_{21}-1)R_b}{i_{21}} = 0 . \tag{14}$$

And the equation of plane involute C_2 on gear 2 is

Table 1. Parameters of plane involute pair.

Parameters	Values
Module *m*/(mm)	6
Pressure angle *α*/(°)	20
Tooth number of gear 1 z_1	17
Tooth number of internal gear 2 z_2	68
Transmission ratio i_{21}	4
Pitch circle radius of gear 1 R_1/(mm)	51
Pitch circle radius of internal gear 2 R_2/(mm)	204
Basis circle radius of gear 1 R_{b1}/(mm)	47.92
Basis circle radius of internal gear 2 R_{b2}/(mm)	191.48
Central distance *a*/(mm)	153
Involute generating angle *θ*/(rad)	0~π/2

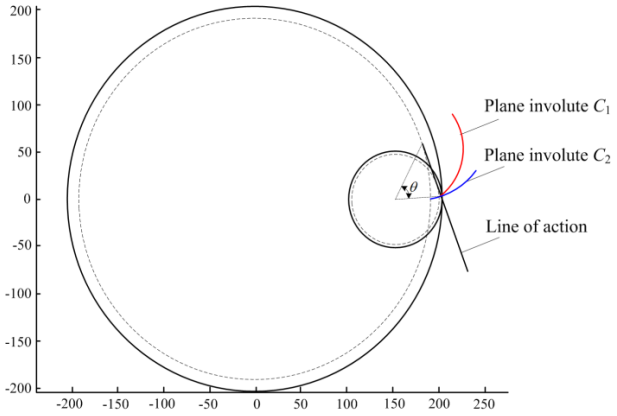

Fig. 4. Meshing scheme of plane involute pair.

$$\begin{cases}x_{i2} = R_b\cos[(1-i_{21})\varphi_1+\theta] + R_b\theta\sin[(1-i_{21})\varphi_1+\theta] \\ \qquad - a\cos(i_{21}\varphi_1) \\ y_{i2} = R_b\sin[(1-i_{21})\varphi_1+\theta] - R_b\theta\cos[(1-i_{21})\varphi_1+\theta] \\ \qquad + a\cos(i_{21}\varphi_1) \\ z_{i2} = 0 \\ \varphi_1 = \arccos\dfrac{(i_{21}-1)R_b}{i_{21}} - \theta .\end{cases} \tag{15}$$

The line of action can also be derived as

$$\begin{cases}x_{la} = R_b\cos(\varphi_1+\theta) + R_b\theta\sin(\varphi_1+\theta) \\ y_{la} = R_b\sin(\varphi_1+\theta) - R_b\theta\cos(\varphi_1+\theta) \\ z_{la} = 0 .\end{cases} \tag{16}$$

Given the parameters in Table 1, we get the meshing scheme of plane involute pair using MATLAB software. The results are displayed in Fig. 4. Plane involute C_1 and C_2 mesh at a point and the line of action is the common tangent of the basis circles of two gears. It is also the common normal of plane involutes at the contact point. The results conform to the general involute characteristics and it verifies the feasible of the proposed principle.

(2) Spatial cylindrical helical curve

Similarly, the spatial cylindrical helical curves are chosen for consideration and expressed as

$$\begin{cases} x_{c1} = r\cos\theta_c \\ y_{c1} = r\sin\theta_c \\ z_{c1} = p\theta_c \end{cases} \tag{17}$$

where r is the pitch circle radius of spatial cylindrical helical curve. θ_c is angle parameter of spatial cylindrical helical curve and p is helix parameter.

The meshing equation is deduced as follows according to Eq. (10).

$$\lambda_1 \sin(\theta_c + \varphi_1) = \frac{\lambda_2 p}{(r^2+p^2)^{\frac{1}{2}}} - \frac{\lambda_2 p}{(r^2+p^2)^{\frac{1}{2}}}\cos(\theta_c + \varphi_1). \tag{18}$$

Its conjugated spatial curve and the line of action are also obtained as

$$\begin{cases} x_{c2} = r\cos[(1-i_{21})\varphi_1 + \theta_c] - a\cos(i_{21}\varphi_1) \\ y_{c2} = r\sin[(1-i_{21})\varphi_1 + \theta_c] + a\cos(i_{21}\varphi_1) \\ z_{c2} = p\theta_c \\ \sin(\theta_c + \varphi_1) = \dfrac{\lambda_2 p}{\lambda_1 (r^2+p^2)^{\frac{1}{2}}} - \dfrac{\lambda_2 p}{\lambda_1 (r^2+p^2)^{\frac{1}{2}}}\cos(\theta_c + \varphi_1), \end{cases} \tag{19}$$

and

$$\begin{cases} x_{line} = r\cos(\varphi_1 + \theta_c) \\ y_{line} = r\sin(\varphi_1 + \theta_c) \\ z_{line} = p\theta_c . \end{cases} \tag{20}$$

Given the parameters in Table 2, the meshing scheme of spatial cylindrical helical curves is drawn using MATLAB software. The results are shown in Fig. 5.

Two spatial cylindrical helical curves mesh in point contact and the line of action is a spatial straight line passing through the contact point. During the engagement motion, the contact point located on the conjugate curves moves along the line of action. The results show that these paired curves can satisfy the continuous motion and meshing conditions. The feasibility of the basic principle is further verified.

2.2 Tooth profiles modeling

The conjugate curve theory shows that a pair of conjugate curves have continuous and tangent motion in the given contact direction. Based on equidistant-enveloping generation, the tooth surfaces can be obtained in terms of the designated conjugate curves.

The equidistant-enveloping principle is shown in Fig. 6. General plane equidistant from curve T_1 to curve T_2 is displayed in Fig. 6(a). The curve T_2 is obtained through the motion of curve T_1 along the designated locus with distance L. For spatial equidistant in Fig. 6(b), the designated normal direction $\boldsymbol{n}$ in space curve trihedron is given and curve W_1 is the original curve. Curves W_2 and W_3 are the corresponding equidistant curve of curve W_1 with distance l_1 and l_2 in different normal direction, respectively. They can be expressed as

$$W_2 : \begin{cases} x_{W_2} = x_{W_1} + l_1 \cdot \boldsymbol{n}_x \\ y_{W_2} = y_{W_1} + l_1 \cdot \boldsymbol{n}_y \\ z_{W_2} = z_{W_1} + l_1 \cdot \boldsymbol{n}_z , \end{cases} \tag{21}$$

and

Table 2. Parameters of spatial cylindrical helical curves.

Parameters	Values
Pitch circle radius of spatial cylindrical helical curve 1 r_1/(mm)	120
Pitch circle radius of spatial cylindrical helical curve 2 r_2/(mm)	24
Central distance a/(mm)	96
Transmission ratio i_{21}	5
Helix angle β/(°)	26.68
Angle parameter of spatial cylindrical helical curve θ_c/(rad)	-0.2~0.2
Angle parameter λ_1	-cos25°
Angle parameter λ_2	-sin25°

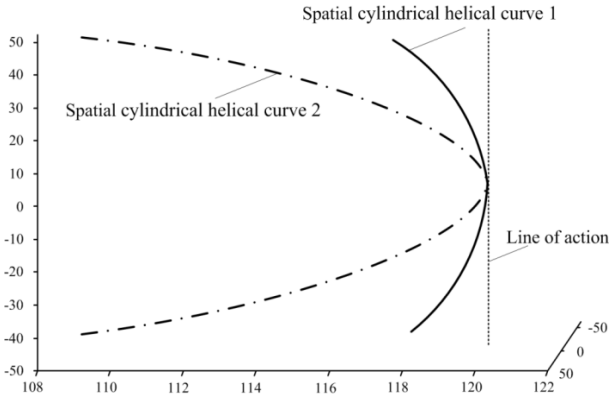

Fig. 5. Meshing scheme of spatial cylindrical helical curve.

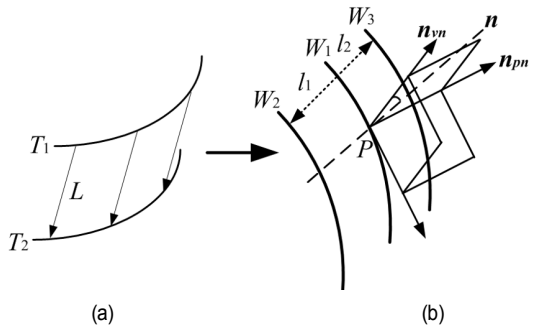

Fig. 6. Equidistant-enveloping principle: (a) plane equidistant; (b) spatial equidistant.

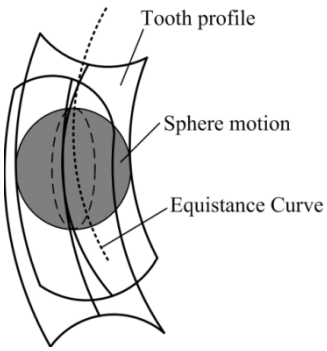

Fig. 7. Tooth profiles generation.

$$W_3:\begin{cases} x_{W_3}=x_{W_1}+l_2\cdot \boldsymbol{n}_x \\ y_{W_3}=y_{W_1}+l_2\cdot \boldsymbol{n}_y \\ z_{W_3}=z_{W_1}+l_2\cdot \boldsymbol{n}_z . \end{cases} \tag{22}$$

Generation of tooth profiles is further developed by sphere enveloping motion, as shown in Fig. 7. The center of the selected sphere moves along the equidistant curve and the tooth profile can be obtained according to the enveloping method if given the parameter range.

So an internal gear pair which has the single contact point between the mated gears can be developed. Equations of tooth profiles of internal gear pair are written as

$$\Omega_1:\begin{cases} x_{\Omega 1}=x_{W_2}+l_1\cos\varphi\cos\alpha \\ y_{\Omega 1}=y_{W_2}+l_1\cos\varphi\sin\alpha \\ z_{\Omega 1}=z_{W_2}+l_1\sin\varphi \\ \Delta(\varphi,\alpha,t)=(\dfrac{\partial\Omega_1}{\partial\alpha}\times\dfrac{\partial\Omega_1}{\partial\varphi})\cdot\dfrac{\partial\Omega_1}{\partial t}=0 \\ \dfrac{\partial\Omega_1}{\partial\alpha}=\{-l_1\cos\varphi\sin\alpha,l_1\cos\varphi\cos\alpha,0\} \\ \dfrac{\partial\Omega_1}{\partial\varphi}=\{-l_1\sin\varphi\cos\alpha,-l_1\sin\varphi\sin\alpha,l_1\cos\varphi\} \\ \dfrac{\partial\Omega_1}{\partial t}=\{x'_{W_2},y'_{W_2},z'_{W_2}\}, \end{cases} \tag{23}$$

and

$$\Omega_2:\begin{cases} x_{\Omega 2}=x_{W_3}+l_2\cos\varphi'\cos\alpha' \\ y_{\Omega 2}=y_{W_3}+l_2\cos\varphi'\sin\alpha' \\ z_{\Omega 2}=z_{W_3}+l_2\sin\varphi' \\ \Delta(\varphi',\alpha',t')=(\dfrac{\partial\Omega_2}{\partial\alpha'}\times\dfrac{\partial\Omega_2}{\partial\varphi'})\cdot\dfrac{\partial\Omega_2}{\partial t'}=0 \\ \dfrac{\partial\Omega_2}{\partial\alpha'}=\{-l_2\cos\varphi'\sin\alpha',l_2\cos\varphi'\cos\alpha',0\} \\ \dfrac{\partial\Omega_2}{\partial\varphi'}=\{-l_2\sin\varphi'\cos\alpha',-l_2\sin\varphi'\sin\alpha',l_2\cos\varphi'\} \\ \dfrac{\partial\Omega_2}{\partial t'}=\{x'_{W_3},y'_{W_3},z'_{W_3}\} \end{cases} \tag{24}$$

where φ,α and φ',α' are the sphere surface parameters. t and t' are curve parameters.

Furthermore, we utilize the example with spatial cylindrical helical curve. Based on Eqs. (17) and (19), the equidistant curves can be calculated. And they have

$$\begin{cases} x_{W_2}=r\cos\theta_c+l_1\dfrac{n_{x_1}}{\sqrt{n_{x_1}^2+n_{y_1}^2+n_{z_1}^2}} \\ y_{W_2}=r\sin\theta_c+l_1\dfrac{n_{y_1}}{\sqrt{n_{x_1}^2+n_{y_1}^2+n_{z_1}^2}} \\ z_{W_2}=p\theta_c+l_1\dfrac{n_{z_1}}{\sqrt{n_{x_1}^2+n_{y_1}^2+n_{z_1}^2}}, \end{cases} \tag{25}$$

and

$$\begin{cases} x_{W_3}=r\cos[(1-i_{21})\varphi_1+\theta_c]-a\cos(i_{21}\varphi_1)+l_2\dfrac{n_{x_2}}{\sqrt{n_{x_2}^2+n_{y_2}^2+n_{z_2}^2}} \\ y_{W_3}=r\sin[(1-i_{21})\varphi_1+\theta_c]+a\cos(i_{21}\varphi_1)+l_2\dfrac{n_{y_2}}{\sqrt{n_{x_2}^2+n_{y_2}^2+n_{z_2}^2}} \\ z_{W_3}=p\theta_c+l_2\dfrac{n_{z_2}}{\sqrt{n_{x_2}^2+n_{y_2}^2+n_{z_2}^2}}. \end{cases} \tag{26}$$

The relationship between parameters φ_1 and θ_c can be derived by Eq. (18). Substituting Eqs. (25) and (26) into Eqs. (23) and (24), respectively, we can obtain the tooth surfaces of internal gear pair as follows.

$$\Omega_1:\begin{cases} x_{\Omega 1}=r\cos\theta_c+l_1\dfrac{n_{x_1}}{\sqrt{n_{x_1}^2+n_{y_1}^2+n_{z_1}^2}}+l_1\cos\varphi\cos\alpha \\ y_{\Omega 1}=r\sin\theta_c+l_1\dfrac{n_{y_1}}{\sqrt{n_{x_1}^2+n_{y_1}^2+n_{z_1}^2}}+l_1\cos\varphi\sin\alpha \\ z_{\Omega 1}=p\theta_c+l_1\dfrac{n_{z_1}}{\sqrt{n_{x_1}^2+n_{y_1}^2+n_{z_1}^2}}+l_1\sin\varphi \\ \Delta(\varphi,\alpha,t)=(\dfrac{\partial\Omega_1}{\partial\alpha}\times\dfrac{\partial\Omega_1}{\partial\varphi})\cdot\dfrac{\partial\Omega_1}{\partial t}=0, \end{cases} \tag{27}$$

and

$$\Omega_2:\begin{cases} x_{\Omega 2}=r\cos[(1-i_{21})\varphi_1+\theta_c]-a\cos(i_{21}\varphi_1)+l_2\dfrac{n_{x_2}}{\sqrt{n_{x_2}^2+n_{y_2}^2+n_{z_2}^2}} \\ \qquad +l_2\cos\varphi'\cos\alpha' \\ y_{\Omega 2}=r\sin[(1-i_{21})\varphi_1+\theta_c]+a\cos(i_{21}\varphi_1)+l_2\dfrac{n_{y_2}}{\sqrt{n_{x_2}^2+n_{y_2}^2+n_{z_2}^2}} \\ \qquad +l_2\cos\varphi'\sin\alpha' \\ z_{\Omega 2}=p\theta_c+l_2\dfrac{n_{z_2}}{\sqrt{n_{x_2}^2+n_{y_2}^2+n_{z_2}^2}}+l_2\sin\varphi' \\ \Delta(\varphi',\alpha',t')=(\dfrac{\partial\Omega_2}{\partial\alpha'}\times\dfrac{\partial\Omega_2}{\partial\varphi'})\cdot\dfrac{\partial\Omega_2}{\partial t'}=0 . \end{cases} \tag{28}$$

Table 3. Parameters of internal tooth surfaces.

Parameters	Values
Pitch circle radius of spatial cylindrical helical curve 1 r_1/(mm)	100
Pitch circle radius of spatial cylindrical helical curve 2 r_2/(mm)	20
Central distance a/(mm)	80
Normal module m_n/(mm)	6
Transmission ratio i_{21}	5
Helix angle β/(°)	25.84
Normal equidistance of spatial cylindrical helical curve 1 l_1/(mm)	4.8
Normal equidistance of spatial cylindrical helical curve 2 l_2/(mm)	4
Tooth number of internal gear 1	30
Tooth number of small gear 2	6
Angle parameter of spatial cylindrical helical curve θ_c/(rad)	-0.15~0.15
Angle parameter λ_1	-cos30°
Angle parameter λ_2	-sin30°
Tooth width B/(mm)	60

Given parameters values in Table 3, internal tooth surface examples are developed and the drawing results with MATLAB software are displayed in Fig. 8.

Fig. 8 shows contact conditions of internal meshing tooth surfaces. At different times, the contact point moves along the action of line, and contact point of tooth surfaces is also the contact point of spatial cylindrical helical conjugate-curves. It satisfies the continuous and correct transmission conditions.

3. Solid modeling

UG and MATLAB software are used for establishing solid models of internal gear pair, due to the special gear tooth. Based on theoretical derivations of tooth surfaces, programming with MATLAB software for generation of tooth surfaces can be obtained. Further, 3D tooth surfaces can be generated through the import data points utilizing surface building function provided by UG software. According to the design parameters of gears, dimension trimming and surface stitching can be carried out to generate a gear model, and using array and Boolean operation, the complete gear model can be obtained.

According to the parameters in Table 3, the final internal meshing gear models are displayed in Fig. 9. Specially, tooth number of the pinion is only six and it is smaller than the minimum tooth number of general involute gear for avoiding undercutting condition. Using motion analysis module of UG software, the rotation internal gear pair with a given speed ratio is set up. During this process, no tooth profile interference occurs and only a contact point is located on the mated tooth profiles. The motion locus moves continuously along the axial direction.

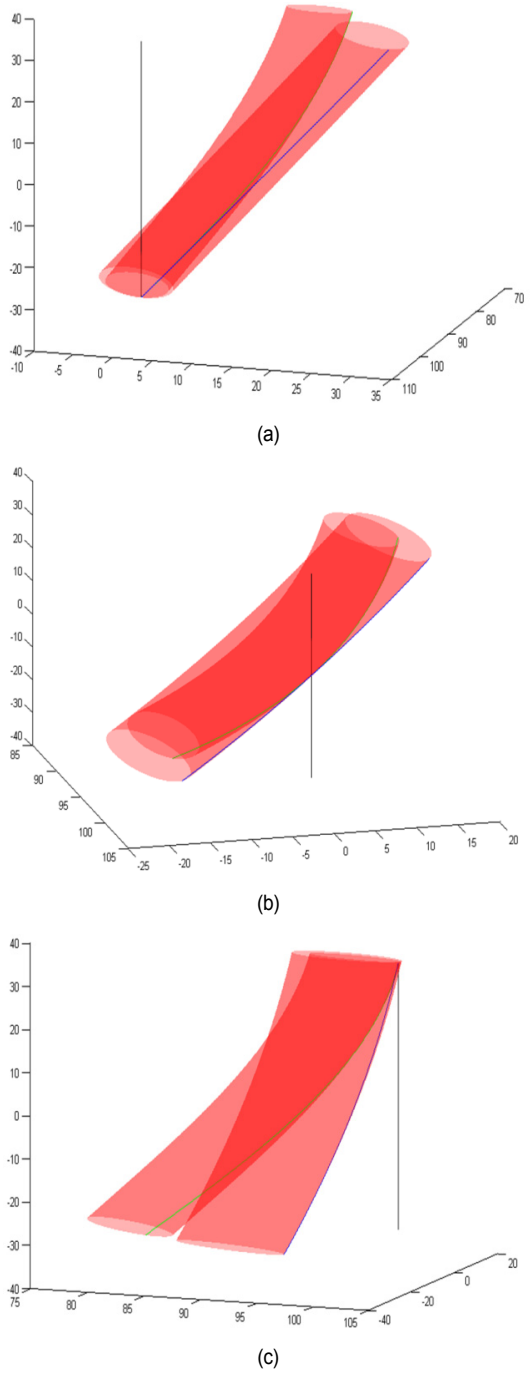

Fig. 8. Internal meshing tooth surfaces (unit: mm): (a) beginning position; (b) middle position; (c) end position.

4. Meshing analysis

Usually the contact point is elastically deformed if the gear teeth are loaded and it can expand from a contact point to a contact area, which is beneficial to increase the load capacity of the gear teeth. Here, we use FEA method to analysis the tooth profiles contact. The surface-to-surface contact element is utilized to simulate the contact condition between complex

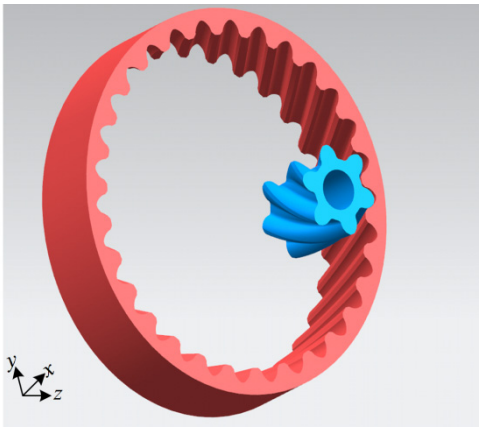

(a)

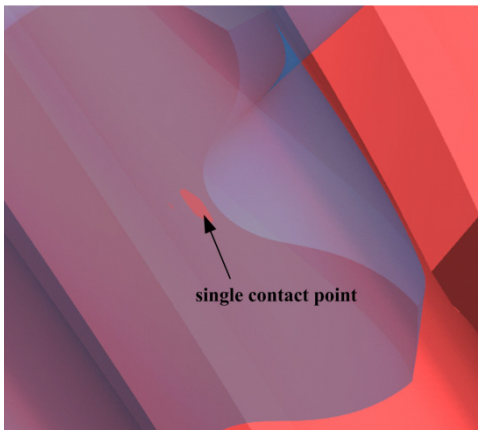

(b)

Fig. 9. Internal gear models: (a) gear pair; (b) single contact point.

surfaces, and it is a high-order contact element [21-23].

4.1 Stress analysis with single contact point

Based on the gear models established in Sec. 3, considering the factors of element size and computer operation efficiency, single tooth was selected for FEA process to solve the results. The internal gear pair was imported into ANSYS software to generate element and node models. After several trial calculations, we determined that the unit size of the contact surface was 0.2*0.2 mm and the element type was Solid 186. The numbers of units and nodes are 357464 and 1538978, respectively. The length unit in ANSYS software was set to millimeter for our analysis process. Also, the mass and time units were set to kilogram and second, respectively. Gear pair material was selected to be 40Cr alloy steel, where its tensile strength was 980 Mpa and yield limit was 785 Mpa, and the elastic modulus of the material was E = 2.06*10^5 MPa. The Poisson ratio was set to be μ = 0.3. According to the setting of ANSYS software, tooth profile of the pinion was chosen as the contact surface, and tooth profile of the internal gear was chosen as the target surface. It is an asymmetric contact and the frictional coefficient is 0.2. To eliminate the initial clearance between

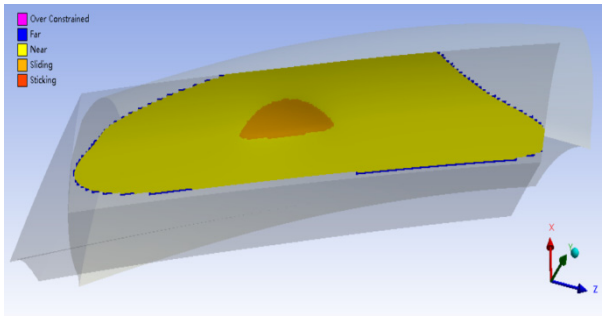

(a)

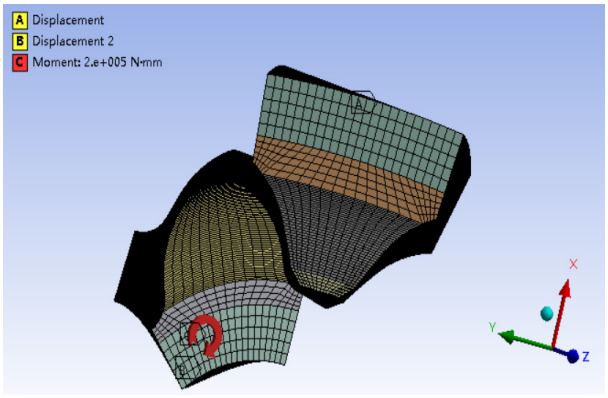

(b)

Fig. 10. Finite element model of internal gear pair with single contact point: (a) contact condition; (b) finite element analysis model.

tooth profiles, the contact units were also set to adjust to touch.

Each node has translational freedom in three directions of UX, UY and UZ. To carry out the analysis of tooth contact, we needed to consider the interaction and deformation conditions between the tooth surfaces, so it was necessary to fix the outer surface of the internal gear. Furthermore, perfect constraints were imposed on the nodes of the outer surface of the internal gear (UX = UY = UZ = 0). And constraints were imposed on the degrees of freedom of all nodes on the inner surface of the pinion along the directions of UX and UZ, i.e., radial and axial directions (UX = UZ = 0).

The finite element model of internal gears with single tooth is shown in Fig. 10. We analyzed the contact conditions of tooth profiles based on the setting conditions. The input torque applied to the inner surface of pinion was 200 Nm. Loading time was 1s and the time sub steps were set to 5. Stress analysis results of the internal gears with single contact point are displayed in Figs. 11-13.

From the analysis results in Fig. 11, the maximum contact stress between the internal gear pair is 1429.4 MPa. The maximum stress occurs at contact point, which is located on the middle of the tooth profile. It has regular elliptical distribution along the direction of tooth width, and the distribution area has the trend of expanding to the tooth root direction. With the increase of the contact area, the contact stress will gradually decrease. The maximum von Mises stress and shear stress of the pinion with single contact point in Fig. 12 are 729.02 MPa

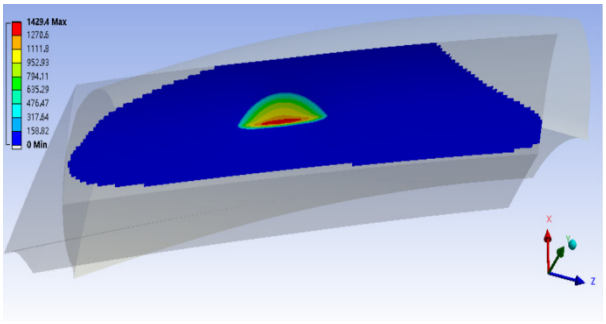

Fig. 11. Contact stress of internal gear pair with single contact point (unit: MPa).

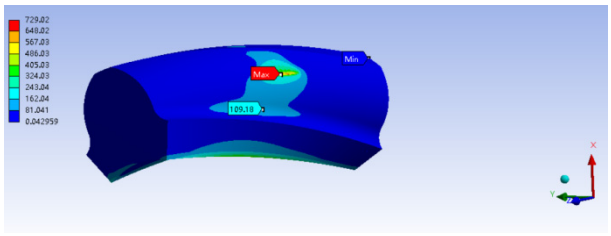

(a)

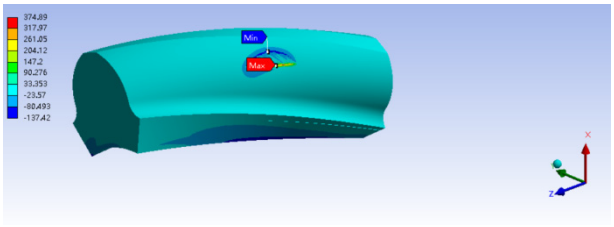

(b)

Fig. 12. Stress analysis results of the pinion with single contact point (unit: MPa): (a) von Mises stress; (b) shear stress.

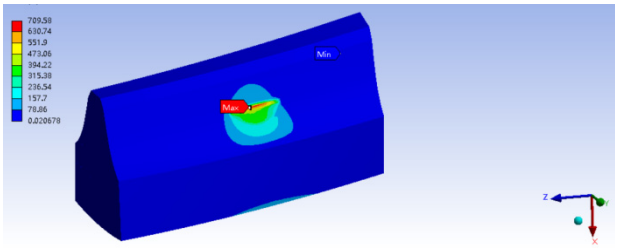

(a)

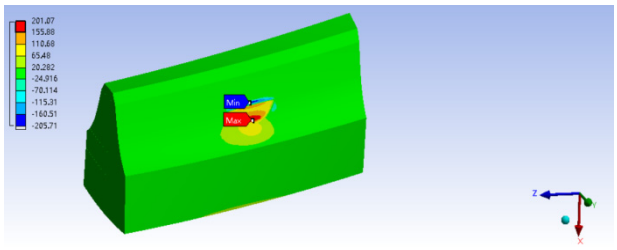

(b)

Fig. 13. Stress analysis results of the internal gear with single contact point (unit: MPa): (a) von Mises stress; (b) shear stress.

and 374.89 MPa, respectively. The maximum von Mises stress and shear stress of the internal gear with single contact point in Fig. 13 are 729.58 MPa and 201.07 MPa, respectively.

4.2 Stress analysis with two contact points

Similarly, we established a gear model with two contact points according to the proposed generation methods of tooth profiles. It means that there are two contact points on one contact pair at the same time during the meshing process. Here, the meshing pair should also be the pinion with convex tooth profile and the internal gear with concave tooth profile. According to the derived conclusions in Sec. 2, we can obtain tooth surfaces of internal gear pair with two contact points as follows.

$$\Omega_{1t}:\begin{cases} x_{\Omega 1t}=r\cos\theta_c+l_{1t}\dfrac{n_{x_1}}{\sqrt{n_{x_1}^2+n_{y_1}^2+n_{z_1}^2}}+l_{1t}\cos\varphi_t\cos\alpha_t \\ y_{\Omega 1t}=r\sin\theta_c+l_{1t}\dfrac{n_{y_1}}{\sqrt{n_{x_1}^2+n_{y_1}^2+n_{z_1}^2}}+l_{1t}\cos\varphi_t\sin\alpha_t \\ z_{\Omega 1t}=p\theta_c+l_{1t}\dfrac{n_{z_1}}{\sqrt{n_{x_1}^2+n_{y_1}^2+n_{z_1}^2}}+l_{1t}\sin\varphi_t \\ \Delta(\varphi_t,\alpha_t,t_t)=(\dfrac{\partial\Omega_{1t}}{\partial\alpha_t}\times\dfrac{\partial\Omega_{1t}}{\partial\varphi_t})\cdot\dfrac{\partial\Omega_{1t}}{\partial t_t}=0, \end{cases} \tag{29}$$

and

$$\Omega_{2t_1}:\begin{cases} x_{\Omega 2t_1}=r\cos[(1-i_{21})\varphi_1+\theta_c]-a\cos(i_{21}\varphi_1) \\ \quad +l_{2t}\dfrac{n_{x_2}}{\sqrt{n_{x_2}^2+n_{y_2}^2+n_{z_2}^2}}+l_{2t}\cos\varphi_t'\cos\alpha_t' \\ y_{\Omega 2t_1}=r\sin[(1-i_{21})\varphi_1+\theta_c]+a\cos(i_{21}\varphi_1) \\ \quad +l_{2t}\dfrac{n_{y_2}}{\sqrt{n_{x_2}^2+n_{y_2}^2+n_{z_2}^2}}+l_{2t}\cos\varphi_t'\sin\alpha_t' \\ z_{\Omega 2t_1}=p\theta_c+l_{2t}\dfrac{n_{z_2}}{\sqrt{n_{x_2}^2+n_{y_2}^2+n_{z_2}^2}}+l_{2t}\sin\varphi_t' \\ \Delta(\varphi_t',\alpha_t',t_t')=(\dfrac{\partial\Omega_{2t}}{\partial\alpha_t'}\times\dfrac{\partial\Omega_{2t}}{\partial\varphi_t'})\cdot\dfrac{\partial\Omega_{2t}}{\partial t_t'}=0 \end{cases} \tag{30}$$

$$\Omega_{2t_2}:\begin{cases} x_{\Omega 2t_2}=r\cos[(1-i_{21})\varphi_1+\theta_c]-a\cos(i_{21}\varphi_1) \\ \quad +l_{2t}\dfrac{n_{x_2}(\Delta\delta)}{\sqrt{n_{x_2}^2(\Delta\delta)+n_{y_2}^2(\Delta\delta)+n_{z_2}^2(\Delta\delta)}} \\ \quad +l_{2t}\cos\varphi_t''\cos\alpha_t'' \\ y_{\Omega 2t_2}=r\sin[(1-i_{21})\varphi_1+\theta_c]+a\cos(i_{21}\varphi_1) \\ \quad +l_{2t}\dfrac{n_{y_2}(\Delta\delta)}{\sqrt{n_{x_2}^2(\Delta\delta)+n_{y_2}^2(\Delta\delta)+n_{z_2}^2(\Delta\delta)}} \\ \quad +l_{2t}\cos\varphi_t''\sin\alpha_t'' \\ z_{\Omega 2t_2}=p\theta_c+l_{2t}\dfrac{n_{z_2}(\Delta\delta)}{\sqrt{n_{x_2}^2(\Delta\delta)+n_{y_2}^2(\Delta\delta)+n_{z_2}^2(\Delta\delta)}} \\ \quad +l_{2t}\sin\varphi_t'' \\ \Delta(\varphi_t'',\alpha_t'',t_t'')=(\dfrac{\partial\Omega_{2t}}{\partial\alpha_t''}\times\dfrac{\partial\Omega_{2t}}{\partial\varphi_t''})\cdot\dfrac{\partial\Omega_{2t}}{\partial t_t''}=0. \end{cases} \tag{31}$$

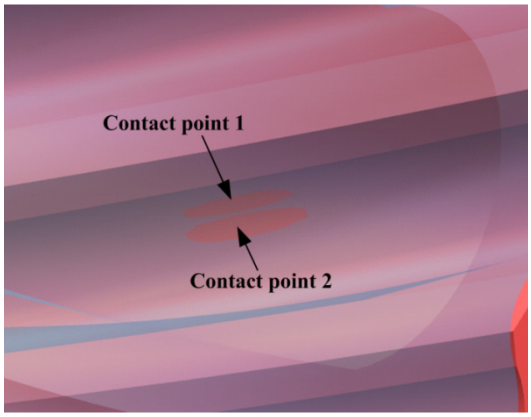

Fig. 14. Internal gear model with two contact points.

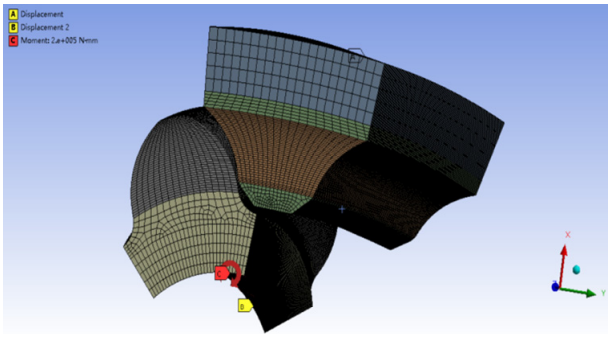

Fig. 15. Finite element model of internal gear pair with two contact points.

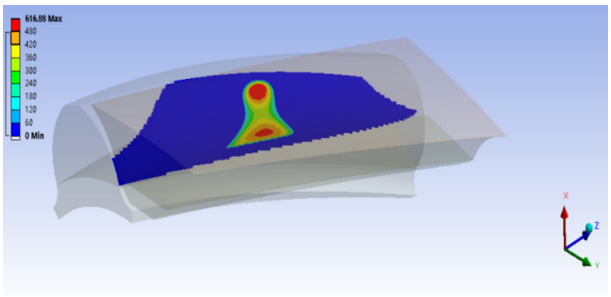

Fig. 16. Contact stress of internal gear pair with two contact points (unit: MPa).

Based on solid modeling methods in Sec. 3, the internal gear models with two contact points can be established as shown in Fig. 14. For its stress analysis, the contact unit size, material properties, boundary conditions and load application are the same with gears with single contact point. The numbers of units and nodes are 378644 and 1608008, respectively.

Finite element model of internal gears with two contact points is shown in Fig. 15. The analysis results in Fig. 16 show that the maximum contact stress of internal gears with two contact points is 616.88 MPa. The maximum von Mises stress and shear stress of the pinion with two contact points in Fig. 17 are 417.21 MPa and 133.82 MPa, respectively. The maximum von

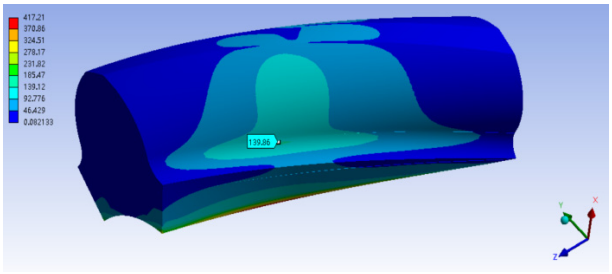

(a)

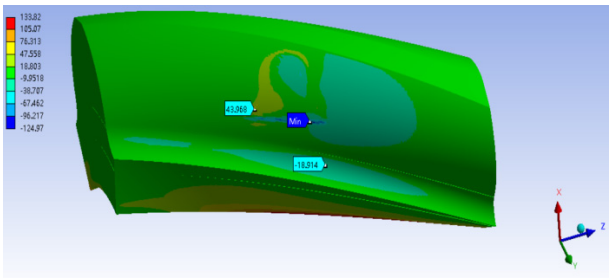

(b)

Fig. 17. Stress analysis results of the pinion with two contact points (unit: MPa): (a) von Mises stress; (b) shear stress.

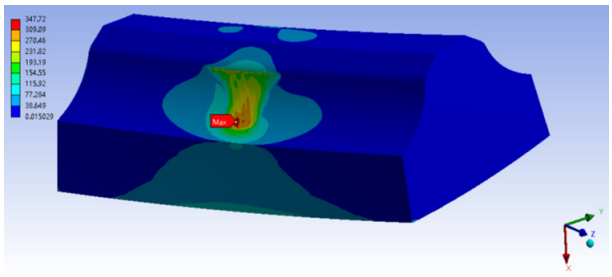

(a)

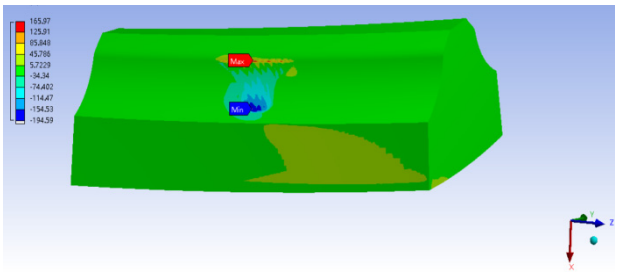

(b)

Fig. 18. Stress analysis results of the internal gear with two contact points (unit: MPa): (a) von Mises stress; (b) shear stress.

Mises stress and shear stress of the internal gear with two contact points in Fig. 18 are 347.72 MPa and 165.97 MPa, respectively.

Obviously, two peak stress regions can be found on tooth profiles, which are also corresponding to two contact points. The stress distribution area is relatively concentrated and it has the trends of expanding towards the tooth root direction. The maximum contact stress of tooth profiles with two contact

points is 56.8 % lower than that of tooth profiles with single point contact. The maximum von Mises stress and shear stress of the pinion with two contact points are, respectively, 42.7 % and 64.3 % lower than that of the pinion with single point contact. The maximum von Mises stress and shear stress of the internal gear with two contact points are, respectively, 52.3 % and 17.4 % lower than that of the internal gear with single point contact. It has an advantage in the load capacity of gear tooth profiles and has good application prospect in engineering.

5. Conclusions

1) A new internal meshing gear transmission with curve element is proposed based on conjugate curve theory. For a given spatial curve, the meshing equation and its conjugated spatial curve under the motion law were derived. Considering the equidistant kinematic method, general internal tooth profile models were established by the conjugate-curve pair. The results further confirm the feasibility and correctness of the developed meshing principle applied to internal gear transmission. It also provides a theoretical basis for the follow-up study of novel gears.

2) A numerical example of internal gear pair was developed in terms of given parameters. We obtained the drawings of the spatial conjugate curves and tooth surfaces using the image function of MATLAB software. The results verify the theoretical derivation and general design thought. Solid models were further obtained by MATLAB and UG software. Motion simulation result shows that the gear pair satisfies point contact condition and design requirements.

3) Meshing analysis of tooth profiles using FEA method was carried out. Contact unit, material property, boundary conditions and basic constraints were introduced. Two kinds of tooth profiles with point contact were analyzed. The analysis results show that the maximum contact stress, maximum von Mises stress and shear stress of tooth profiles with two contact points are lower than those of tooth profiles with single point contact. This has an advantage in the load capacity of gear tooth profiles. Further studies on transmission characteristics and manufacturing technology of the new gear drive will be carried out.

Acknowledgments

The research is supported by National Key Research and Development Program of China (Grant No. 2018YFB2001300), National Natural Science Foundation of China (Grant No. 51975078), Fundamental and Frontier Research Project of Chongqing (Grant No. cstc2018jcyjAX0029), Science and Technology Research Program of Chongqing Municipal Education Commission (Grant No. KJQN201900736) and Chongqing Key Laboratory of Urban Rail Transit System Integration and Control Open Fund (Grant No. CKLURTSIC-KFKT-202005). The financial support is gratefully acknowledged. The authors would like to thank the editor and reviewers for review of this manuscript.

References

[1] A. Singh, A. Kahraman and H. Ligata, Internal gear strains and load sharing in planetary transmissions: model and experiments, *J. of Mechanical Design*, 130 (7) (2008) 917-928.

[2] F. L. Litvin and A. Fuentes, *Gear Geometry and Applied Theory*, 2nd Ed., Cambridge University Press, Cambridge (2004).

[3] S. C. Yang, Study on an internal gear with asymmetric involute teeth, *Mechanism and Machine Theory*, 42 (8) (2007) 977-994.

[4] Y. H. Chen, G. H. Zhang, B. K. Chen and W. J. Luo, A novel enveloping worm pair via employing the conjugating planar internal gear as counterpart, *Mechanism and Machine Theory*, 67 (9) (2013) 17-31.

[5] J. R. Cho, K. Y. Jeong, M. H. Park and D. S. Shin, Finite element structural analysis of wind turbine gearbox considering tooth contact of internal gear system, *J. of Mechanical Science and Technology*, 27 (7) (2013) 2053-2059.

[6] M. S. Tunalioglu and B. Tuc, Theoretical and experimental investigation of wear in internal gears, *Wear*, 309 (1-2) (2014) 208-215.

[7] T. H. Pham, L. Müller and J. Weber, Dynamically loaded the ring gear in the internal gear motor/pump: mobility method solution, *J. of Mechanical Science and Technology,* 32 (7) (2018) 3023-3035.

[8] T. H. Pham and J. Weber, Theoretical and experimental analysis of the effect of misaligned ring gear on performance of internal gear motors/pumps, *J. of Mechanical Science and Technology*, 33 (9) (2019) 4049-4060.

[9] Y. Y. Liu, Research on gear shaping strategy for internal helical non-circular gears and performance analyses for linkage models, *J. of Mechanical Science and Technology*, 28 (7) (2014) 2749-2757.

[10] X. C. Gui, X. Q. Zhan, P. Ye and H. X. Li, Design and analysis of internal compound cycloid gear transmission with high contact ratio, *J. of Mechanical Engineering*, 53 (1) (2017) 55-64 (in Chinese).

[11] Y. Yanase, M. Komori and M. Ochi, Grinding of internal gears by setting a large crossed-axes angle using a barrel-shaped grinding wheel, *Precision Engineering*, 52 (4) (2018) 384-391.

[12] K. Uriu, T. Osafune, T. Murakami and M. Nakamura, Effects of shaft angle on cutting tool parameters in internal gear skiving, *J. of Mechanical Science and Technology*, 31 (12) (2017) 5665-5673.

[13] J. Han and G. Z. Zhang, Investigation on formation mechanism of surface texture and modeling of surface roughness with internal gear power honing, *The International J. of Advanced Manufacturing Technology*, 98 (9) (2018) 603-615.

[14] B. K. Chen, D. Liang and Y. E. Gao, The principle of conjugate curves for gear transmission, *J. of Mechanical Engineering*, 50 (1) (2014) 130-136 (in Chinese).

[15] R. L. Tan, B. K. Chen, C. Y. Peng and X. Li, Study on spatial curve meshing and its application for logarithmic spiral bevel gears, *Mechanism and Machine Theory*, 86 (4) (2015) 172-190.

[16] D. Liang, B. K. Chen and Y. E. Gao, Theoretical and experimental investigations on parallel-axis gear transmission with

tubular meshing surfaces, *International J. of Precision Engineering and Manufacturing*, 16 (10) (2015) 2147-2157.

[17] Y. E. Gao, B. K. Chen and D. Liang, Mathematical models of hobs for conjugate-curve gears having three contact points, *Proceedings of the Institution of Mechanical Engineers, Part C: J. of Mechanical Engineering Science*, 229 (13) (2015) 2402-2411.

[18] B. K. Chen, D. Liang and Z. Y. Li, A study on geometry design of spiral bevel gears based on conjugate curves, *International J. of Precision Engineering and Manufacturing*, 15 (3) (2014) 477-482.

[19] D. Liang, B. K. Chen and Y. E. Gao, Hobbing manufacturing of new type of involute-helix gears for wind turbine gearbox, *International J. of Precision Engineering and Manufacturing – Green Technology*, 6 (1) (2019) 305-313.

[20] S. Feng, L. H. Chang and Z. X. He, A hybrid finite element and analytical model for determining the mesh stiffness of internal gear pairs, *J. of Mechanical Science and Technology*, 34 (59) (2020) 2477-2485.

[21] A. Fuentes, R. Ruiz-Orzaez and I. Gonzalez-Perez, Computerized design, simulation of meshing, and finite element analysis of two types of geometry of curvilinear cylindrical gears, *Computer Methods in Applied Mechanics and Engineering*, 272 (4) (2014) 321-339.

[22] S. Y. Liu, C. S. Song, C. C. Zhu, C. C. Liang and X. Y. Yang, Investigation on the influence of work holding equipment errors on contact characteristics of face-hobbed hypoid gear, *Mechanism and Machine Theory*, 138 (8) (2019) 95-111.

[23] C. C. Liang, C. S. Song, C. C. Zhu, Y. W. Wang, S. Y. Liu and R. H. Sun, Investigation of tool errors and their influences on tooth surface topography for face-hobbed hypoid gears, *J. of Mechanical Design*, 142 (4) (2020) 1-11.

Dong Liang received his Ph.D. in Mechanical Design and Theory from Chongqing University, China. He also spent two years as a postdoctoral researcher at Chongqing University, China. He currently works in School of Mechanotronics & Vehicle Engineering at Chongqing Jiaotong University, China. His research areas of interest include gear design, optimization and manufacturing.

Weibin Li received his M.S. in Mechanical Design and Theory from Chongqing University, China. His research areas of interest include gear design and manufacturing.

Bingkui Chen is currently a Professor for the State Key Lab of Mechanical Transmissions at Chongqing University, China. He is also a Vice Director of the CMES Gear Technical Committee. Prof. Chen has conducted pioneering research related to gear geometry, kinematics, dynamics and manufacturing.